Research Square

Preprints are preliminary reports that have not undergone peer review.
They should not be considered conclusive, used to inform clinical practice,
or referenced by the media as validated information.

Unlocking Volcanic Swarms: Swarm-Informed ETAS and Plastic Rock Deformation

Anna Tramelli

anna.tramelli@ingv.it

INGV - Sezione di Napoli Osservatorio Vesuviano https://orcid.org/0000-0001-6259-5730

Cataldo Godano

Department of Mathematics and Physics, University of Campania

Vincenzo Convertito

INGV https://orcid.org/0000-0002-7115-7502

Giuseppe Petrillo

CNRS, ENS de Lyon https://orcid.org/0000-0002-2339-559X

Article

Keywords: Swarm Informed ETAS model, Time and space kernels, Plastic deformation, Volcanic swarms

Posted Date: October 15th, 2026

DOI: https://doi.org/10.21203/rs.3.rs-11268830/v1

License: This work is licensed under a Creative Commons Attribution 4.0 International License.
Read Full License

Additional Declarations: There is **NO** Competing Interest.

Unlocking Volcanic Swarms: Swarm-Informed ETAS and Plastic Rock Deformation

Cataldo Godano[1†], Vincenzo Convertito[2†], Anna Tramelli[2*†], Giuseppe Petrillo[3†]

[1]Department of Mathematics and Physics, University of Campania, Viale Lincoln 5, Caserta, 81100, Italy.
[2]INGV, Osservatorio Vesuviano, Via Diocleziano 328, Napoli, 80125, Italy.
[3]CNRS, ENS de Lyon, LPENSL, UMR5672, Lyon, 69342, France.

*Corresponding author(s). E-mail(s): anna.tramelli@ingv.it;
Contributing authors: cataldo.godano@unicampania.it;
vincenzo.convertito@ingv.it; giuseppe51289@gmail.com;
†These authors contributed equally to this work.

Abstract

Earthquake swarms on volcanoes are critical precursors to eruptions, reflecting the complex interplay between rock deformation, hydrothermal or magmatic fluid migration, and fault activation. Standard Epidemic-Type Aftershock Sequence (ETAS) models often fail to accurately replicate these sequences because their scale-free triggering kernels do not account for the distinct, time-bound, and spatially restricted clustering typical of volcanic environments. To address these limitations, this study introduces the Swarm-Informed ETAS (SIETAS) model. The SIETAS framework incorporates a modified temporal kernel where the standard power-law decay features an exponential cutoff governed by a characteristic relaxation time, alongside a normalized generalized isotropic spatial kernel motivated by the cored and sigmoidal spatial organization observed in stacked volcanic swarms. The SIETAS model was applied to comprehensive seismic catalogs from six volcanic systems worldwide: Bárðarbunga, Etna, Hawaii (Mauna Loa–Kīlauea), Nevado del Ruiz, Vesuvius, and Yellowstone. For five of the six analyzed catalogues, the presented SIETAS solutions yield lower negative log-likelihood, AIC, and BIC values than standard ETAS. To establish a physical mechanism for this Gamma-like seismic rate decay, we introduce a simple frictional two-block model where deformation occurs via velocity-strengthening stable creep. The strong agreement between the analytical formulation and

empirical results confirms that swarm seismicity is governed by a deformation-controlled, self-exciting triggering process linked to Andrade-type transient creep.

Keywords: Swarm Informed ETAS model, Time and space kernels, Plastic deformation, Volcanic swarms

Introduction

Earthquake swarms provide a window into the processes that redistribute stress within volcanic and hydrothermal systems. Unlike classical mainshock-aftershock sequences, they develop without a single dominant mainshock and may involve multiple earthquakes of comparable magnitude [1–3]. Their temporal evolution and spatial organization offer complementary information on the interplay between earthquake triggering, fluid migration and aseismic deformation. A central challenge is to represent these features within a common framework that allows quantitative comparison across volcanic systems.

Earthquake activity is seldom uniform over time, frequently presenting as localized bursts or intervals of accelerated seismicity [3, 4]. These swarms are mostly confined to limited geographical regions and regularly emerge near active fault systems, geothermal areas, or volcanic centers [5, 6]. Unlike standard mainshock-aftershock sequences, which are chiefly driven by stress redistribution on the fault and/or coseismic stress transfer, swarms represent the response of a fault network to external transient perturbations [7, 8]. The underlying driving mechanisms include fluid-induced pore-pressure diffusion [9, 10], magmatic or hydrothermal fluid transport within volcanic zones [11–13], and slow aseismic slip that progressively loads small locked asperities [14–17].

Volcanic swarms are frequently characterized by transient activation phases, recurring seismic bursts, and spatial clustering associated with hydrothermal and magmatic systems. Although standard ETAS kernels include characteristic temporal and spatial scales, their prescribed decay shapes may limit their ability to reproduce these features. In particular, the modified Omori kernel lacks an intrinsic exponential taper, while the standard spatial kernel constrains the shape of the transition between its central region and its power-law tail. We therefore test whether introducing an exponential temporal taper and an additional spatial shape parameter improves the description of seismicity at six volcanic systems relative to standard ETAS. Indeed, empirical kernels for volcanic earthquakes often deviate from standard tectonic models. Specifically, temporal triggering decays as a power law with an exponential cutoff [18]. A recent analysis of stacked volcanic-earthquake swarms showed that the distribution of distances from the largest events of each swarm is characterized by an approximately uniform short-distance regime followed by a rapid decay [19]. This empirical profile was represented by the logistic relation

$$p_{\mathrm{G}}(\delta) = \frac{k}{1 + \exp[\alpha(\delta - \delta_0)]}, \tag{1}$$

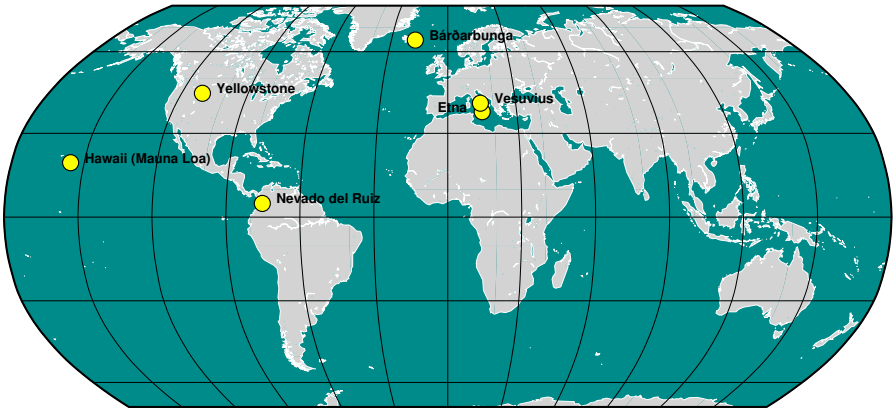


Fig. 1 Global geographic framework of the six volcanic systems analyzed in this study. Yellow circles mark the locations of the magmatic and hydrothermal complexes investigated: Bárðarbunga (Iceland), Etna (Italy), Hawaii/Mauna Loa–Kīlauea (USA), Nevado del Ruiz (Colombia), Vesuvius (Italy), and Yellowstone (USA).

where δ is the epicentral distance between the largest-magnitude earthquake in each swarm and the other events belonging to that swarm, δ_0 is the transition distance, and α controls the exponential decay at large distances. Equation (1), however, is a phenomenological one-dimensional distribution of distances measured from the largest-magnitude event of each previously identified swarm. It is therefore not directly equivalent to an ETAS triggering kernel, which must describe the normalized two-dimensional distribution of offspring around every potential parent earthquake. Motivated by the cored and sigmoidal structure identified by Godano and Petrillo [19], we introduce an ETAS-compatible powered-logistic profile in logarithmic distance. This formulation has an exact two-dimensional normalization, allows the characteristic triggering length to depend on parent magnitude, and contains the standard ETAS spatial kernel as a particular case. We hereafter refer to the ETAS model incorporating this specific kernel as the Swarm-Informed ETAS (SIETAS) model. The SIETAS framework has previously been utilized to characterize the temporal distribution of earthquakes in the Taupo Volcanic Zone [20].

We apply SIETAS to six volcanic systems worldwide: Bárðarbunga, Etna, Hawaii (Mauna Loa-Kilauea), Nevado del Ruiz, Vesuvius, and Yellowstone (see Fig. 1 for the volcanoes locations). The current likelihood-based comparison favors SIETAS for five systems, while the Hawaii fit requires further numerical refinement before a model-selection conclusion can be drawn.

1 Data and Methods

The Bárðarbunga catalogue spans the interval 2009.003–2016.000 in decimal years. The input file contains 42741 earthquakes; 43 records that could not be parsed were excluded. Using a completeness magnitude $m_c = 0.7$, $N = 13594$ earthquakes were retained for likelihood estimation.

The Etna catalogue contains 10151 earthquakes and spans the interval 2019.003–2025.002 in decimal years. Using $m_c = 2.2$, $N = 429$ earthquakes were retained for likelihood estimation.

The Hawaii catalogue contains 109743 earthquakes and spans the interval 2010.005–2024.014 in decimal years. Using $m_c = 2.3$, $N = 56555$ earthquakes were retained for likelihood estimation.

The Nevado del Ruiz catalogue contains 6981 earthquakes and spans the interval 2018.162–2026.430 in decimal years. Using $m_c = 1.9$, $N = 1049$ earthquakes were retained for likelihood estimation.

The Vesuvius catalogue contains 8797 located earthquakes and spans the interval 1998.015–2023.686 in decimal years. Each record contains occurrence time, latitude, longitude, depth, and magnitude. Using $m_c = -0.2$, $N = 8319$ earthquakes were retained for spatio-temporal likelihood estimation.

The Yellowstone catalogue contains 38860 earthquakes and spans the interval 2010.003–2024.012 in decimal years. Using $m_c = 2.0$, $N = 6431$ earthquakes were retained for likelihood estimation.

Figure 2 shows the epicentral distributions of the six catalogues, with symbol size indicating magnitude and colour indicating focal depth.

We assess the completeness magnitude (m_c) of each catalogue using the variability coefficient (c_V) method [21], calculated as the ratio between the standard deviation and the mean of the magnitudes. Because the Gutenberg–Richter law [22] follows an exponential distribution for $m \geq m_c$, the corresponding variability coefficient is $c_V = 1$. Consequently, we evaluate c_V against a threshold magnitude m_{th} (for $m \geq m_{th}$). If $m_{th} \geq m_c$, the distribution aligns with the Gutenberg–Richter law and $c_V \to 1$; otherwise, catalogue incompleteness leads to $c_V \neq 1$. In practice, m_c is defined as the minimum threshold magnitude for which the variability coefficient reaches the prescribed value:

$$m_c = \min \left\{ m_{\text{th}} : c_V(m_{\text{th}}) \geq c_V^{\text{th}} \right\}. \tag{2}$$

While Godano et al. [23] recommended $c_V^{th} = 0.73$ based on numerical simulations, we found that a higher threshold ($c_V^{th} = 0.9$) is more appropriate for small-scale areas to avoid underestimating m_c.

1.1 Standard and swarm-informed ETAS models

Let the earthquake catalogue be represented by $\{(t_i, \mathbf{x}_i, m_i)\}_{i=1}^{N}$, where t_i is the occurrence time, $\mathbf{x}_i \in \mathcal{W}$ is the epicentral position inside the spatial observation window $\mathcal{W}$, and $m_i \geq m_c$ is the magnitude. We denote by T the duration of the catalogue, by $|\mathcal{W}|$ the area of the observation window, and define

$$\Delta m_i = m_i - m_c.$$

Both the standard ETAS model [24**?** –27] and the swarm-informed ETAS (SIETAS) model [20] are formulated as marked spatio-temporal self-exciting point

processes. Their conditional intensity is

$$\lambda(t, \mathbf{x} \mid \mathcal{H}_t) = \frac{\mu}{|\mathcal{W}|} + \sum_{\substack{i: t_i < t \\ 0 < t - t_i \le H}} K \exp(\alpha \Delta m_i)\, g(t - t_i)\, f(\|\mathbf{x} - \mathbf{x}_i\| \mid m_i), \qquad (3)$$

where $\mathcal{H}_t$ denotes the history of the process up to time t. The parameter μ is the total background rate over $\mathcal{W}$, $K \exp(\alpha \Delta m_i)$ is the productivity of event i, and H is the maximum triggering-history length. The background is assumed to be uniform in space. Both spatial kernels are isotropic; therefore, no preferred propagation direction or anisotropy is included.

For the standard ETAS model, the normalized temporal triggering kernel is the modified Omori law

$$g_{\mathrm{E}}(t) = \frac{(t + c)^{-p}}{Z_{\mathrm{E}}(H)}, \qquad 0 < t \le H, \qquad (4)$$

where

$$Z_{\mathrm{E}}(H) = \int_0^H (u + c)^{-p}\, du = \frac{c^{1-p} - (c + H)^{1-p}}{p - 1}. \qquad (5)$$

When the complete triggering history is used, $H = \infty$, so that

$$Z_{\mathrm{E}}(\infty) = \frac{c^{1-p}}{p - 1},$$

which requires $p > 1$.

The SIETAS temporal kernel introduces a characteristic relaxation time τ:

$$g_{\mathrm{S}}(t) = \frac{\exp(-t/\tau)(t + c)^{-p}}{Z_{\mathrm{S}}(H)}, \qquad 0 < t \le H, \qquad (6)$$

with

$$Z_{\mathrm{S}}(H) = \int_0^H \exp(-u/\tau)(u + c)^{-p}\, du. \qquad (7)$$

This kernel behaves approximately as a power law at short and intermediate times and is exponentially suppressed for $t \gtrsim \tau$. Unlike the infinite-horizon Omori kernel, it remains integrable for $p \le 1$ because of the exponential taper. The standard temporal kernel is recovered in the limiting case $\tau \to \infty$.

In both models, the characteristic spatial length depends on the magnitude of the triggering earthquake:

$$L_i = L(m_i) = r_c \exp(\gamma_s \Delta m_i), \qquad (8)$$

where r_c is a reference length and γ_s controls the magnitude dependence of the triggering distance.

The standard ETAS spatial density is

$$f_{\mathrm{E}}(r \mid m_i) = \frac{q - 1}{\pi L_i^2} \left[1 + \left(\frac{r}{L_i} \right)^2 \right]^{-q}, \qquad q > 1, \qquad (9)$$

which is normalized over the infinite plane.

1.1.1 Relation to the empirical logistic swarm profile

The empirical relation proposed by Godano and Petrillo [19], was obtained from the stacked one-dimensional distributions of the radial distances between the largest-magnitude earthquake and the other events belonging to each previously identified swarm. Here δ_0 represents the transition distance between the short-distance regime and the exponentially decaying regime, while α controls the far-field exponential decay.

This empirical distance distribution cannot be inserted unchanged into an ETAS conditional intensity. Indeed, an isotropic ETAS kernel $f(r)$ is a probability density per unit area around every potential parent earthquake. Its associated radial-distance density is

$$p_R(r) = 2\pi r f(r). \tag{10}$$

Therefore, $p_{\mathrm{G}}(r)$ and $f(r)$ are densities with respect to different probability measures. Directly identifying them would mix a one-dimensional radial density with a two-dimensional areal density. Conversely, the literal conversion

$$f_{\mathrm{G}}(r) = \frac{p_{\mathrm{G}}(r)}{2\pi r}$$

would produce an integrable but singular areal density at $r = 0$.

We therefore retain the characteristic spatial scale and the smooth core-to-tail transition suggested by the empirical analysis, while introducing a regular two-dimensional density suitable for ETAS likelihood estimation. The SIETAS spatial kernel is

$$f_{\mathrm{S}}(r \mid m_i) = \frac{b}{2\pi L_i^2 B(2/b, \kappa/b)} \left[1 + \left(\frac{r}{L_i}\right)^b\right]^{-\nu}, \tag{11}$$

where

$$L_i = r_c \exp[\gamma_s(m_i - m_c)], \qquad \nu = \frac{2+\kappa}{b}, \qquad b > 0, \quad \kappa > 0. \tag{12}$$

Here $B(\cdot,\cdot)$ is the beta function. The condition

$$b\nu = 2 + \kappa > 2$$

guarantees normalization over the two-dimensional plane:

$$2\pi \int_0^\infty r f_{\mathrm{S}}(r \mid m_i)\, dr = 1. \tag{13}$$

The connection with the empirical logistic profile becomes apparent by rewriting the attenuation factor as

$$\left[1 + \left(\frac{r}{L_i}\right)^b\right]^{-\nu} = \left[1 + \exp\left\{b \log\left(\frac{r}{L_i}\right)\right\}\right]^{-\nu}. \tag{14}$$

Thus, the empirical relation in Eq. (1) is logistic in linear distance, whereas the SIETAS attenuation is a powered-logistic function in logarithmic distance. Both formulations introduce a central spatial scale and a smooth transition toward the far field, but they do not have the same asymptotic tail.

At short distances, the SIETAS areal density behaves as

$$f_{\mathrm{S}}(r \mid m_i) \simeq f_{\mathrm{S}}(0 \mid m_i) \left[1 - \nu \left(\frac{r}{L_i}\right)^b\right], \qquad r \ll L_i, \tag{15}$$

whereas at large distances

$$f_{\mathrm{S}}(r \mid m_i) \propto r^{-b\nu} = r^{-(2+\kappa)}, \qquad r \gg L_i. \tag{16}$$

By comparison, the empirical logistic profile satisfies

$$p_{\mathrm{G}}(r) \propto \exp(-\alpha r) \qquad \text{for } r \gg \delta_0.$$

The SIETAS kernel should therefore be regarded as an ETAS-compatible spatial model motivated by the cored and sigmoidal empirical swarm geometry, rather than as an exact mathematical generalization of the exponential-tail profile proposed by Godano and Petrillo [19].

The half-amplitude radius of the SIETAS areal profile is

$$r_{1/2} = L_i \left(2^{1/\nu} - 1\right)^{1/b}. \tag{17}$$

This quantity plays a role analogous to the empirical transition distance δ_0, although the two are not expected to coincide because they refer to different spatial statistics.

Finally, the standard ETAS spatial kernel is recovered by setting

$$b = 2, \qquad \nu = q, \qquad \kappa = 2(q-1). \tag{18}$$

Together with the temporal limit $\tau \to \infty$, this shows that standard ETAS is nested within SIETAS. This property permits a direct likelihood-based comparison between the two models.

1.2 Likelihood, boundary correction, and optimization

For a spatio-temporal point process observed over $[0, T] \times \mathcal{W}$, the log-likelihood is

$$\ell(\boldsymbol{\theta}) = \sum_{j=1}^{N} \log \lambda(t_j, \mathbf{x}_j \mid \mathcal{H}_{t_j}) - \int_0^T \int_{\mathcal{W}} \lambda(t, \mathbf{x} \mid \mathcal{H}_t)\, d\mathbf{x}\, dt, \tag{19}$$

where $\boldsymbol{\theta}$ is the vector of model parameters.

Using the normalization of the temporal and spatial kernels, Eq. (19) can be written as

$$\ell(\boldsymbol{\theta}) = \sum_{j=1}^{N} \log \lambda(t_j, \mathbf{x}_j \mid \mathcal{H}_{t_j}) - \mu T - \sum_{i=1}^{N} K \exp(\alpha \Delta m_i)\, G(u_i)\; Q_i, \tag{20}$$

where

$$u_i = \min(T - t_i, H), \qquad G(u) = \int_0^u g(t)\, dt, \tag{21}$$

and

$$Q_i = \int_{\mathcal{W}} f(\|\mathbf{x} - \mathbf{x}_i\| \mid m_i)\, d\mathbf{x} \tag{22}$$

is the fraction of the spatial triggering density falling inside the observation window. The factors $G(u_i)$ and Q_i correct, respectively, for the finite end of the catalogue and for spatial boundary losses.

Epicentral coordinates were projected onto a local Cartesian system in kilometres. In the numerical implementation, $\mathcal{W}$ was defined as the axis-aligned rectangular bounding box of the projected epicentres. The spatial integral Q_i was evaluated by angular quadrature. If $R_i(\phi)$ is the distance from event i to the rectangular boundary along direction ϕ, then

$$Q_i \simeq \frac{1}{N_\phi} \sum_{k=1}^{N_\phi} F_R(R_i(\phi_k) \mid m_i)\,, \tag{23}$$

where F_R is the radial cumulative distribution. For standard ETAS,

$$F_{R,\mathrm{E}}(R \mid m_i) = 1 - \left[1 + \left(\frac{R}{L_i}\right)^2\right]^{1-q}, \tag{24}$$

whereas for SIETAS

$$F_{R,\mathrm{S}}(R \mid m_i) = I_z\left(\frac{2}{b}, \frac{\kappa}{b}\right), \qquad z = \frac{(R/L_i)^b}{1 + (R/L_i)^b}, \tag{25}$$

and $I_z(a, b)$ is the regularized incomplete beta function. Final likelihood values were evaluated using $N_\phi = 64$ angular directions.

For numerical stability, productivity was parameterized in terms of a catalogue-averaged nominal branching ratio n_b:

$$K = \frac{n_b}{N^{-1} \sum_{i=1}^{N} \exp(\alpha \Delta m_i)}. \tag{26}$$

Under full temporal and spatial normalization, n_b is the mean number of direct offspring averaged over the empirical magnitude sample. Because the observed window excludes offspring occurring outside $\mathcal{W}$, the expected number observed inside the catalogue is generally smaller than n_b.

The standard spatio-temporal model has eight fitted parameters,

$$\boldsymbol{\theta}_{\mathrm{E}} = (\mu, n_b, \alpha, c, p, r_c, q, \gamma_s),$$

whereas SIETAS has ten:

$$\boldsymbol{\theta}_{\mathrm{S}} = (\mu, n_b, \alpha, c, p, \tau, r_c, b, \kappa, \gamma_s).$$

All six catalogues used in the final model comparison contain epicentral coordinates. The standard ETAS and SIETAS models therefore contain eight and ten fitted parameters, respectively, for every volcanic system, including Vesuvius.

Parameters were mapped to an unconstrained space by logarithmic or logistic transformations and the negative log-likelihood, $\mathrm{NLL} = -\ell$, was minimized with the Nelder-Mead algorithm. For the largest catalogues, the first optimization stage used a weighted subsample of target events while retaining all potential parent events within H.

Model support was evaluated using

$$\mathrm{AIC} = 2k - 2\ell_{\max}, \qquad \mathrm{BIC} = k \log N - 2\ell_{\max}, \tag{27}$$

where k is the number of fitted parameters. Lower AIC and BIC values indicate greater support after penalizing model complexity.

2 ETAS-SIETAS comparison

Table 1 reports the best solutions returned by the current numerical optimization. SIETAS attained lower NLL, AIC, and BIC values than standard ETAS for Bárðarbunga, Etna, Nevado del Ruiz, Vesuvius, and Yellowstone. For Hawaii, the current SIETAS optimization returned a larger NLL than standard ETAS. Because standard ETAS is contained in SIETAS as a limiting case, this result indicates that the current SIETAS solution is not a valid global optimum. Model selection for Hawaii is therefore considered numerically inconclusive pending a multistart optimization initialized from the embedded standard-ETAS solution.

The fitted nominal branching ratios were close to the imposed upper bound $n_b = 0.99$ for several catalogues. In addition, the standard ETAS fit for Vesuvius reached the lower bound $p \simeq 1.001$. These boundary solutions indicate that parameter uncertainties and the sensitivity to m_c, H, and the spatial observation window should be investigated before assigning a direct physical interpretation to the individual parameter estimates.

All the values of the fitted parameters are reported in tables 2 and 3 respectively for ETAS and SIETAS models.

Table 1 Comparison between standard ETAS and SIETAS. Here k denotes the number of fitted parameters. Lower NLL, AIC, and BIC values indicate greater statistical support. All comparisons are spatio-temporal. The dagger identifies the current Hawaii SIETAS solution as a local numerical solution requiring further multistart optimization.

Volcanic system	Model	m_c	N	k	NLL	AIC	BIC
Bárðarbunga	ETAS	0.7	13594	8	16207.524	32431.047	32491.186
	SIETAS	0.7	13594	10	16190.837	32401.675	32476.849
	ΔBIC = −14.338	In favor of SIETAS					
Etna	ETAS	2.2	429	8	3151.654	6319.307	6351.799
	SIETAS	2.2	429	10	3135.985	6291.971	6332.585
	ΔBIC = −19.214	In favor of SIETAS					
Hawaii	ETAS	2.3	56555	8	165077.478	330170.956	330242.500
	SIETAS†	2.3	56555	10	165202.063	330424.127	330513.556
	ΔBIC = 271.056	Current solution; inconclusive					
Nevado del Ruiz	ETAS	1.9	1049	8	11448.267	22912.535	22952.180
	SIETAS	1.9	1049	10	11244.245	22508.490	22558.045
	ΔBIC = −394.134	In favor of SIETAS					
Vesuvius	ETAS	-0.2	8319	8	7822.519	15661.038	15717.248
	SIETAS	-0.2	8319	10	7390.561	14801.122	14871.385
	ΔBIC = −845.863	In favor of SIETAS					
Yellowstone	ETAS	2.0	6431	8	42653.101	85322.203	85376.354
	SIETAS	2.0	6431	10	42631.104	85282.209	85349.898
	ΔBIC = −26.456	In favor of SIETAS					

Table 2 The ETAS parameters estimated for the six volcanoes here analyzed.

Parameter	Bárðarbunga	Etna	Hawaii	Nevado del Ruiz	Vesuvio	Yellowstone
μ	0.0766	0.0592	0.0828	0.1422	0.00215	0.0905
K	0.768	0.804	0.947	0.723	0.866	0.868
n_b	0.99	0.99	0.98	0.99	0.99	0.99
α	0.6	0.54	0.11	0.76	0.18	0.28
c	0.0013	0.002	0.52	0.055	0.002	0.05
p	1.06	1.1	1.33	1.07	1.0	1.06
r_c	0.12	0.69	0.33	1.41	0.2	0.41
q	1.42	1.59	1.44	1.55	2.24	1.33
γ_s	0.021	$2.65{\cdot}10^{-5}$	0.16	$3.74{\cdot}10^{-6}$	0.29	0.0047

2.1 Interpretation of the Nevado del Ruiz spatial parameters

The SIETAS fit for Nevado del Ruiz returned the spatial parameters

$$r_c = 72.40 \text{ km}, \qquad b = 0.5355, \qquad \kappa = 10.265,$$

and therefore

$$\nu = \frac{2+\kappa}{b} = 22.904.$$

Although the value of ν appears anomalously large when considered in isolation, ν is not an independently fitted parameter in the adopted parameterization. Its value is determined by the coupled estimates of b and κ. In particular, the fitted value of b is close to its imposed lower bound, $b_{\min} = 0.5$, which necessarily produces a comparatively large value of ν.

Table 3 Estimated and derived SIETAS quantities for the six volcanic systems. The productivity coefficient K is derived from the fitted nominal branching ratio n_b, whereas $\nu = (2+\kappa)/b$ is derived from b and κ. The symbol ‡ identifies the apparently large value of ν obtained for Nevado del Ruiz, which results from a strongly correlated combination of b, κ, and r_c, as discussed in the text.

Parameter	Bárðarbunga	Etna	Hawaii	Nevado del Ruiz	Vesuvio	Yellowstone
μ	0.037	0.04	0.045	0.073	0.0015	0.092
K	0.79	0.80	0.92	0.80	0.86	0.84
n_b	0.98	0.96	0.98	0.98	0.99	0.96
α	0.53	0.5	0.18	0.52	0.19	0.27
c	0.001	0.0007	0.31	0.00028	0.00023	0.05
p	1.05	0.97	1.14	0.74	0.87	1.06
τ	4102.9	13916.12	195.4	3256.56	5929.62	27644.2
r_c	0.11	0.66	0.32	72.4	0.16	0.45
b	5.69	1.77	2.83	0.54	3.39	4.24
ν	0.47	1.69	0.97	$22.90^{\ddagger}$	1.19	0.61
κ	0.67	1.01	0.73	10.27	2.02	0.59
γ_s	0.093	0.0007	0.1	0.00082	0.32	0.00066

The shape of the SIETAS spatial density is controlled by the combined quantities b, κ, and r_c, rather than by ν alone. Indeed, its far-field behaviour is

$$f_{\mathrm{S}}(r) \propto r^{-b\nu} = r^{-(2+\kappa)}, \qquad r \gg L, \tag{28}$$

so that the fitted areal-density tail for Nevado del Ruiz is approximately

$$f_{\mathrm{S}}(r) \propto r^{-12.265}.$$

The corresponding radial-distance density, $p_R(r) = 2\pi r f_{\mathrm{S}}(r)$, decays as

$$p_R(r) \propto r^{-(1+\kappa)} \simeq r^{-11.265}.$$

The large value of ν therefore expresses, together with the small value of b, a relatively sharp suppression of triggering probability in the far field.

The apparently large reference length r_c should likewise not be interpreted directly as the physical radius of the volcanic swarm. For a triggering earthquake with $m_i = m_c$, the half-amplitude radius of the areal density is

$$r_{1/2} = r_c \left(2^{1/\nu} - 1\right)^{1/b} \simeq 0.108 \text{ km}. \tag{29}$$

Because the radial-distance density additionally contains the two-dimensional Jacobian $2\pi r$, its characteristic distances are larger: the fitted radial mode is approximately 0.79 km, the median triggering distance is approximately 2.97 km, and 90% of the spatial triggering probability lies within approximately 10.86 km. Moreover, the fitted magnitude-scaling coefficient is $\gamma_s = 8.24 \times 10^{-4}$, so that L_i is nearly independent of parent magnitude for this catalogue. For comparison, the standard ETAS fit gives

a radial mode of approximately 0.98 km, a median distance of 2.26 km, and a 90% quantile of 11.48 km. Thus, the central ranges of the ETAS and SIETAS radial distributions are comparable. Their main difference concerns the extreme spatial tail: the 99% radial quantile decreases from approximately 94.65 km for standard ETAS to 27.92 km for SIETAS. The Nevado del Ruiz result therefore indicates that the new kernel suppresses very distant triggering much more strongly, rather than implying an anomalously large physical swarm radius. Nevertheless, the proximity of b to its lower optimization bound and the compensating values of r_c and ν indicate substantial parameter correlation. The individual estimates of these parameters should consequently not be assigned independent physical meanings. Multistart optimization, profile-likelihood analysis, and bootstrap uncertainties are required to determine whether this parameter combination is uniquely identified. The current result supports the fitted spatial probability distribution, but does not by itself establish a specific physical mechanism for the spatial localization of seismicity.

As shown in Figure 3, the comparison between the experimental earthquake occurrence rate and the theoretical rate calculated using the SIETAS model yields an excellent agreement across all six investigated volcanic systems. By computing both rates under an identical 90-day moving window smoothing scheme revealing a consistent match between empirical observations and model curves. Remarkably, this strong fit is visually clear even for the Hawaii (Mauna Loa–Kīlauea) catalog. Although the current numerical solution for Hawaii results in an AIC that statistically favors the standard ETAS model over SIETAS due to ongoing convergence limits, the graphical overlay demonstrates that the physical parameterization of the SIETAS temporal kernel is robust and aligns closely with the actual historical seismicity profile.

3 Mechanical interpretation of the tempered temporal kernel

The temporal evolution of volcanic swarms is commonly characterized by a rapidly decaying initial rate followed by a finite-duration tail. Empirically, this behaviour can be represented by a power-law decay multiplied by an exponential taper [18]. Here we provide a constitutive mechanical interpretation of the temporal kernel adopted in SIETAS. This interpretation is intended to motivate the functional form of the kernel; it is not claimed to constitute a unique microscopic derivation.

Consider a brittle seismogenic block H, with displacement $h(t)$, elastically coupled through a spring of stiffness k to a creeping or viscoelastic block U, with displacement $u(t)$. The latter is driven by an external loading system. This configuration is illustrated schematically in Fig. 4. For additional information see Lippiello et al. [28].

The stress transferred from U to H can be written as

$$\sigma(t) = k\,[u(t) - h(t)]. \tag{30}$$

Outside the short coseismic interval, the displacement of the brittle block may be treated as approximately constant. Consequently,

$$\dot{\sigma}(t) \simeq k\,\dot{u}(t). \tag{31}$$

We represent the transient response of the creeping block by a regularized Andrade-type law,

$$u(t) - u(0) = \begin{cases} \dfrac{A}{1-p}\left[(t+c)^{1-p} - c^{1-p}\right], & p \neq 1, \\ A \log\left(\dfrac{t+c}{c}\right), & p = 1, \end{cases} \tag{32}$$

where $c > 0$ regularizes the response at the origin. Differentiating Eq. (32) gives

$$\dot{u}(t) = A(t+c)^{-p}. \tag{33}$$

For $p = 1$, Eq. (32) corresponds to logarithmic afterslip, whereas values close to $p = 2/3$ are compatible with the strain-rate decay associated with classical Andrade creep [29, 30]. In the statistical model, however, p is estimated from the data and should not automatically be assigned a unique rheological interpretation.

To represent the progressive loss of triggering capacity during a finite swarm, we introduce a time-dependent susceptibility

$$\chi(t) = \chi_0 \exp(-t/\tau), \tag{34}$$

where $\tau > 0$ is the characteristic deactivation or relaxation time. Assuming that the expected number of triggered instabilities per unit stress increment is proportional to $\chi(t)$, the triggering rate generated by a parent earthquake is proportional to

$$\mathcal{R}(t) \propto \chi(t)\,\dot{\sigma}(t) \propto \exp(-t/\tau)(t+c)^{-p}. \tag{35}$$

Equation (35) is precisely the unnormalized temporal shape adopted in the SIETAS conditional intensity. Its two factors have distinct roles: $(t+c)^{-p}$ describes the transient creep-controlled decay, while $\exp(-t/\tau)$ describes the progressive termination of the triggering process. This factorization is a constitutive assumption and should not be interpreted as the consequence of a uniquely determined probability distribution of microscopic failure thresholds.

Over the temporal triggering interval $0 < t \leq H$, the corresponding normalized density is

$$g_{\mathrm{S}}(t) = \frac{\exp(-t/\tau)(t+c)^{-p}}{Z_{\mathrm{S}}(H)}, \tag{36}$$

where

$$Z_{\mathrm{S}}(H) = \int_0^H \exp(-u/\tau)(u+c)^{-p}\,du. \tag{37}$$

Equivalently, this normalization can be written as

$$Z_{\mathrm{S}}(H) = e^{c/\tau}\tau^{1-p}\left[\Gamma\left(1-p, \frac{c}{\tau}\right) - \Gamma\left(1-p, \frac{H+c}{\tau}\right)\right], \tag{38}$$

where $\Gamma(a, x)$ is the upper incomplete gamma function. In the numerical implementation, the integral in Eq. (37) is evaluated numerically, consistently with Eq. (7).

When the characteristic times are well separated, $c \ll \tau$, the unnormalized kernel has the asymptotic behaviour

$$\exp(-t/\tau)(t+c)^{-p} \sim \begin{cases} c^{-p}, & t \ll c, \\ t^{-p}, & c \ll t \ll \tau, \\ t^{-p}\exp(-t/\tau), & t \gg \tau. \end{cases} \tag{39}$$

Thus, c removes the singularity at the origin, p controls the intermediate power-law decay, and τ controls the late exponential taper. The late-time regime is therefore an exponentially tempered power law, rather than a pure exponential or a conventional gamma probability density.

Finally, for a fixed triggering interval H, the standard ETAS temporal kernel is recovered in the limit $\tau \to \infty$:

$$g_{\mathrm{S}}(t) \longrightarrow \frac{(t+c)^{-p}}{\displaystyle\int_0^H (u+c)^{-p}\, du}. \tag{40}$$

For $H = \infty$, this limiting ETAS density is normalizable only when $p > 1$, whereas the exponentially tempered SIETAS kernel remains integrable for every p when $c > 0$ and $\tau > 0$.

4 The origin of the spatial kernel

Here we would like to show as the spatial kernel 11 can be interpreted in terms of damage propagation. For sake of simplicity, in what follows we do not report the normalization factors and make the position $c = \frac{1}{L_i}$ simply because L_i is independent of r. As a consequence we get $f(r) = (1 + (cr)^b)^{-\nu}$ and elevating both members to $-1/\nu$:

$$[f(r)]^{-1/\nu} = 1 + (cr)^b \implies (cr)^b = [f(r)]^{-1/\nu} - 1 \tag{41}$$

Deriving in respect of r and applying the chain rule, we get:

$$\frac{df}{dr} = -\nu\left(1 + (cr)^b\right)^{-\nu-1} \cdot bc(cr)^{b-1} \tag{42}$$

and after some manipulations:

$$\frac{df}{dr} = -\frac{\nu b}{r} f(r) \left(1 - [f(r)]^{1/\nu}\right) \tag{43}$$

and eventually:

$$\frac{df}{d(\ln r)} = -\nu b \cdot f(r) \left(1 - [f(r)]^{1/\nu}\right). \tag{44}$$

In Continuum Damage Mechanics (CDM), the state of a material is described by a damage variable D (representing the cumulative density of micro-fractures in the rock), ranging from 0 (intact material) to 1 (complete failure). The function $f(r)$ represents the residual integrity or reliability of the material $f(r) = 1 - D$.

Substituting $f(r) = 1 - D$ into the differential equation for the standard variant ($\nu = 1$), we obtain the logistic growth equation [31]:

$$\frac{dD}{d(\ln r)} = b \cdot D(1 - D) \tag{45}$$

where r represents the variable driving the damage and $1 - D$ is the portion of material still capable of resisting stresses. The rate of damage growth slows down as the intact material is depleted, or accelerates initially due to stress concentration at existing micro-cracks. The exponent ν (in our case $\nu \neq 1$) introduces an asymmetry into the structural degradation mechanism (generalization), modeling situations in which damage propagates much more rapidly in the final stages compared to the initial ones (or vice versa).

Let us to discuss the different terms of our equation:

- The dependence of the rate on $f(r)$ introduces a feedback mechanism: The volcanic rock is highly fractured. When pressurized fluids enter the system, they reduce the effective normal stress on pre-existing fractures, triggering micro-earthquakes. The change in the medium's integrity (df) at a given distance r depends on how much rock has already been "wetted" or fractured ($1 - f(r)$) and how much rock remains intact ($f(r)$) and capable of offering hydraulic resistance.
- The scale factor r_c (included in L_i) represents a critical distance namely the characteristic size of the seismic swarm [19].
- The exponent b can be viewed as a fracturing index of the rocks and controls the speediness of the rate decay with the distance from the source triggering the swarm occurrence.
- The exponent ν is the Burr Asymmetry [32, 33]: A value of $\nu \neq 1$ indicates that the damage propagation rate does not attenuate symmetrically in respect of the inflection point of the curve. More precisely the curve is skewed generating an heavy tail for $\nu < 1$ and a more rapid decay for $\nu > 1$. Practically speaking a $\nu > 1$ indicates very confined seismicity, whereas $\nu < 1$ indicates a more efficient propagation of the damage in space.

Conclusions

We introduced the Swarm-Informed ETAS model, which modifies both the temporal and spatial triggering kernels of standard ETAS while retaining a uniform spatial background and isotropic triggering. The SIETAS temporal kernel combines a regularized power-law decay with an exponential taper,

$$g_{\mathrm{S}}(t) \propto \exp(-t/\tau)(t+c)^{-p},$$

whereas the spatial kernel is a normalized, magnitude-dependent powered-logistic density,

$$f_{\mathrm{S}}(r \mid m_i) \propto L_i^{-2}\left[1+\left(\frac{r}{L_i}\right)^{b}\right]^{-\nu}, \qquad \nu = \frac{2+\kappa}{b}.$$

Standard ETAS is recovered as a limiting case of this formulation.

The current in-sample likelihood comparison yielded lower NLL, AIC, and BIC values for SIETAS than for standard ETAS for Bárðarbunga, Etna, Nevado del Ruiz, Vesuvius, and Yellowstone. The current Hawaii SIETAS solution returned a larger NLL than standard ETAS. Because standard ETAS is contained in SIETAS as a limiting case, the Hawaii result is interpreted as a local numerical solution rather than as conclusive evidence in favour of standard ETAS. A dedicated multistart optimization is required before model selection can be completed for this catalogue.

The fitted SIETAS relaxation times are substantially longer than the adopted 365-day triggering-history interval for most of the catalogues. Consequently, the exponential temporal taper is weak within the fitted interval in those cases. The present comparison changes the temporal and spatial kernels simultaneously and therefore supports, where favoured by the information criteria, the complete SIETAS specification. It does not isolate how much of the likelihood improvement is attributable to either the temporal or spatial component.

A constitutive two-block model provides a possible mechanical interpretation of the temporal kernel. In this interpretation, regularized Andrade-type transient creep controls the power-law factor, while a progressively decreasing triggering susceptibility produces the exponential taper:

$$\mathcal{R}(t) \propto \chi(t)\dot{\sigma}(t) \propto \exp(-t/\tau)(t+c)^{-p}.$$

This factorization motivates the adopted functional form but does not constitute a unique microscopic derivation. In particular, the fitted values of p and τ should not be interpreted as unambiguous evidence for a specific rheological mechanism. The spatial results indicate that the additional SIETAS shape parameters can accommodate cored triggering distributions with far-field attenuation different from that of standard ETAS. The Nevado del Ruiz fit provides the clearest example of the importance of interpreting the complete spatial distribution rather than an individual parameter. Although the derived value $\nu = 22.904$ is large, it is associated with $b = 0.5355$, $\kappa = 10.265$, and $r_c = 72.40$ km. This coupled parameter combination produces characteristic radial distances comparable to those of standard ETAS over the central part

of the distribution, but a much shorter extreme spatial tail. Therefore, neither r_c nor ν should be interpreted independently as a direct physical length or material property.

Overall, our results indicate that swarm-informed temporal and spatial kernels provide a more flexible statistical description of earthquake clustering in several volcanic catalogues. This improvement suggests that explicitly accounting for swarm-like behaviour may capture features of volcanic seismicity that are not adequately represented by the standard ETAS formulation. However, a better fit does not by itself establish predictive skill. Temporal and spatial residual analyses, together with rigorous out-of-sample testing, are therefore required to determine whether the observed gains translate into improved forecasting performance. Accordingly, SIETAS should be viewed as a flexible statistical framework for characterizing and investigating volcanic-earthquake clustering, rather than as an operational model for eruption-forecasting or monitoring model.

Acknowledgements

VC thanks the project titled D.I.R.E.C.T.I.O.N.S. - Deep learning aIded foReshock deteCTIOn Of iNduced mainShocks, project code: P20220KB4F, CUP: E53D23032910001, PRIN 2022 - Piano Nazionale di Ripresa e Resilienza (PNRR), Mission 4 "Istruzione e Ricerca" - Componente C2 Investimento 1.1, "Fondo per il Programma Nazionale di Ricerca e Progetti di Rilevante Interesse Nazionale (PRIN)." AT, CG and VC thanks the INGV Pianeta Dinamico project HYDROVOLC. GP acknowledges support from the DyDéCo project and from the CPJ Chair at ENS de Lyon and CNRS.

Declarations

Funding This paper was supported by the project Non linear models for magma transport and volcanoes generation - project code: P20222B5P9, PRIN 2022 PNRR.
Conflicts of interest/Competing interests. The authors declare that they have no conflict of interest.
Availability of data and material. The Etna earthquake catalogue is downloadable at the web site https://sismoweb.ct.ingv.it/etna/catalogs/EtnaRCSC/index.php.

The Hawaii and Yellowstone earthquake catalogues can be downloaded at the web site https://earthquake.usgs.gov/earthquakes/search/.

The earthquake catalogue of the Nevado del Ruiz can be downloaded at the web site https://bdrsnc.sgc.gov.co/paginas1/catalogo/index.php

The earthquake catalogue of Vesuvius can be downloaded at the web-site https://www.ov.ingv.it/index.php/bollettini/cataloghi-sismici-1.
Ethical statement The paper is not currently being considered for publication elsewhere.
Author Contribution All the authors equally contributed to the manuscript.

References

[1] Mogi, K.: Some discussions on aftershocks, foreshocks and earthquake swarms:

the relations between some relation between fracture characteristics of laboratory samples and earthquakes. Bulletin of the Earthquake Research Institute, University of Tokyo **41**(3), 615–658 (1963)

[2] Sykes, L.R.: Earthquake swarms and sea-floor spreading. Journal of Geophysical Research **75**(32), 6598–6611 (1970) https://doi.org/10.1029/JB075i032p06598

[3] Vidale, J.E., Shearer, P.M.: A survey of 71 earthquake bursts across southern California: Exploring the role of pore fluid pressure fluctuations and aseismic slip as drivers. Journal of Geophysical Research: Solid Earth **111**(B5) (2006)

[4] Hainzl, S.: Seismicity patterns of earthquake swarms due to fluid intrusion and stress triggering. Geophysical Journal International **159**(3), 1090–1096 (2004)

[5] Hill, D.P.: A model for earthquake swarms. Journal of Geophysical Research **82**(8), 1347–1352 (1977) https://doi.org/10.1029/JB082i008p01347

[6] Passarelli, L., Petersen, G., Mizrahi, L., Cesca, S.: Detecting and Characterizing Swarm-Like Seismicity. Seismological Research Letters **97**(3), 1867–1880 (2026)

[7] Hainzl, S., Ben-Zion, Y., Cattania, C., Wassermann, J.: Testing atmospheric and tidal earthquake triggering at Mt. Hochstaufen, Germany. Journal of Geophysical Research: Solid Earth **118**(10), 5442–5452 (2013)

[8] Petrillo, G., Taroni, M.: Adding strain rate information into a short-term seismicity model improves forecasting performances: the case of Campi Flegrei, Italy. Seismica **4**(2) (2025)

[9] Hubbert, M.K., Rubey, W.W.: Role of fluid pressure in mechanics of overthrust faulting: I. Mechanics of fluid-filled porous solids and its application to overthrust faulting. GSA Bulletin **70**(2), 115–166 (1959)

[10] Ellsworth, W.L.: Injection-induced earthquakes. Science **341**(6142), 1225942 (2013)

[11] Tramelli, A., Godano, C., Ricciolino, P., Giudicepietro, F., Caliro, S., Orazi, M., De Martino, P., Chiodini, G.: Statistics of seismicity to investigate the Campi Flegrei caldera unrest. Scientific reports **11**(1), 7211 (2021)

[12] Tramelli, A., Giudicepietro, F., Ricciolino, P., Chiodini, G.: The seismicity of Campi Flegrei in the contest of an evolving long term unrest. Scientific reports **12**(1), 2900 (2022)

[13] Convertito, V., Godano, C., Petrillo, G., Tramelli, A.: Insights from b value analysis of Campi Flegrei unrests. Scientific Reports **15**(1), 14974 (2025)

[14] Nadeau, R.M., McEvilly, T.V.: Fault slip rates at depth from recurrence intervals of repeating microearthquakes. Science **285**(5428), 718–721 (1999)

[15] Sammis, C.G., Rice, J.R.: Repeating earthquakes as low-stress-drop events at a border between locked and creeping fault patches. Bulletin of the Seismological Society of America **91**(3), 532–537 (2001)

[16] Roland, E., McGuire, J.J.: Earthquake swarms on transform faults. Geophysical Journal International **178**(3), 1677–1690 (2009) https://doi.org/10.1111/j.1365-246X.2009.04214.x

[17] Uchida, N., Bürgmann, R.: Repeating earthquakes. Annual Review of Earth and Planetary Sciences **47**(1), 305–332 (2019)

[18] Godano, C., Tramelli, A., Mora, M.M., Taylor, W., Petrillo, G.: An Analytic Expression for the Volcanic Seismic Swarms Occurrence Rate. A Case Study of Some Volcanoes in the World. Earth and Space Science **10**, 2022–002534 (2023) https://doi.org/10.1029/2022EA002534

[19] Godano, C., Petrillo, G.: Common spatial patterns in earthquake swarms from volcanic systems worldwide. Discover Geoscience **4**(1), 82 (2026)

[20] Petrillo, G., Convertito, V., Tramelli, A., Godano, C.: Seismic Swarms Occurrence Rate and b-value Mapping at Taupo Volcanic Zone. Seismica **5**(1) (2026)

[21] Godano, C., Petrillo, G., Lippiello, E.: Evaluating the incompleteness magnitude using an unbiased estimate of the b value. Geophysical Journal International **236**(2), 994–1001 (2024)

[22] Gutenberg, B., Richter, C.F.: Frequency of earthquakes in California. Bulletin of the Seismological Society of America **34**(4), 185–188 (1944)

[23] Godano, C., Tramelli, A., Petrillo, G., Convertito, V.: Testing the predictive power of b value for Italian seismicity. Seismica **3**(1) (2024)

[24] Ogata, Y.: Statistical Models for Earthquake Occurrences and Residual Analysis for Point Processes. J. Amer. Statist. Assoc. **83**, 9–27 (1988)

[25] Ogata, Y.: Seismicity Analysis through Point-process Modeling: A Review. pure and applied geophysics **155**(2-4), 471–507 (1999) https://doi.org/10.1007/s000240050275

[26] Petrillo, G., Zhuang, J.: Bayesian earthquake forecasting approach based on the epidemic type aftershock sequence model. Earth, Planets and Space **76**(1), 78 (2024)

[27] Petrillo, G., Kumazawa, T., Napolitano, F., Capuano, P., Zhuang, J.: Fluids-triggered swarm sequence supported by a nonstationary epidemic-like description of seismicity. Seismological Research Letters **95**(6), 3207–3220 (2024)

[28] Lippiello, E., Petrillo, G., Landes, F., Rosso, A.: Fault Heterogeneity and the

Connection between Aftershocks and Afterslip. Bulletin of the Seismological Society of America **109**(3), 1156–1163 (2019) https://doi.org/10.1785/0120180244 https://pubs.geoscienceworld.org/bssa/article-pdf/109/3/1156/4710395/bssa-2018244.1.pdf

[29] C. Andrade, E.N.: On the viscous flow in metals, and allied phenomena. Proceedings of the Royal Society of London. Series A, Containing Papers of a Mathematical and Physical Character **84** (1910) https://doi.org/10.1098/rspa.1910.0050

[30] Weiss, J., Amitrano, D.: Logarithmic versus Andrade's transient creep: Role of elastic stress redistribution. Physical Review Materials **7**(3), 033601 (2023)

[31] Liu, D., He, M., Cai, M.: A damage model for modeling the complete stress–strain relations of brittle rocks under uniaxial compression. International Journal of Damage Mechanics **27**(7), 1000–1019 (2018)

[32] Burr, I.W.: Cumulative frequency functions. The Annals of mathematical statistics **13**(2), 215–232 (1942)

[33] Tadikamalla, P.R.: A Look at the Burr and Related Distributions. International Statistical Review **48**(3), 337–344 (1980) https://doi.org/10.2307/1402945

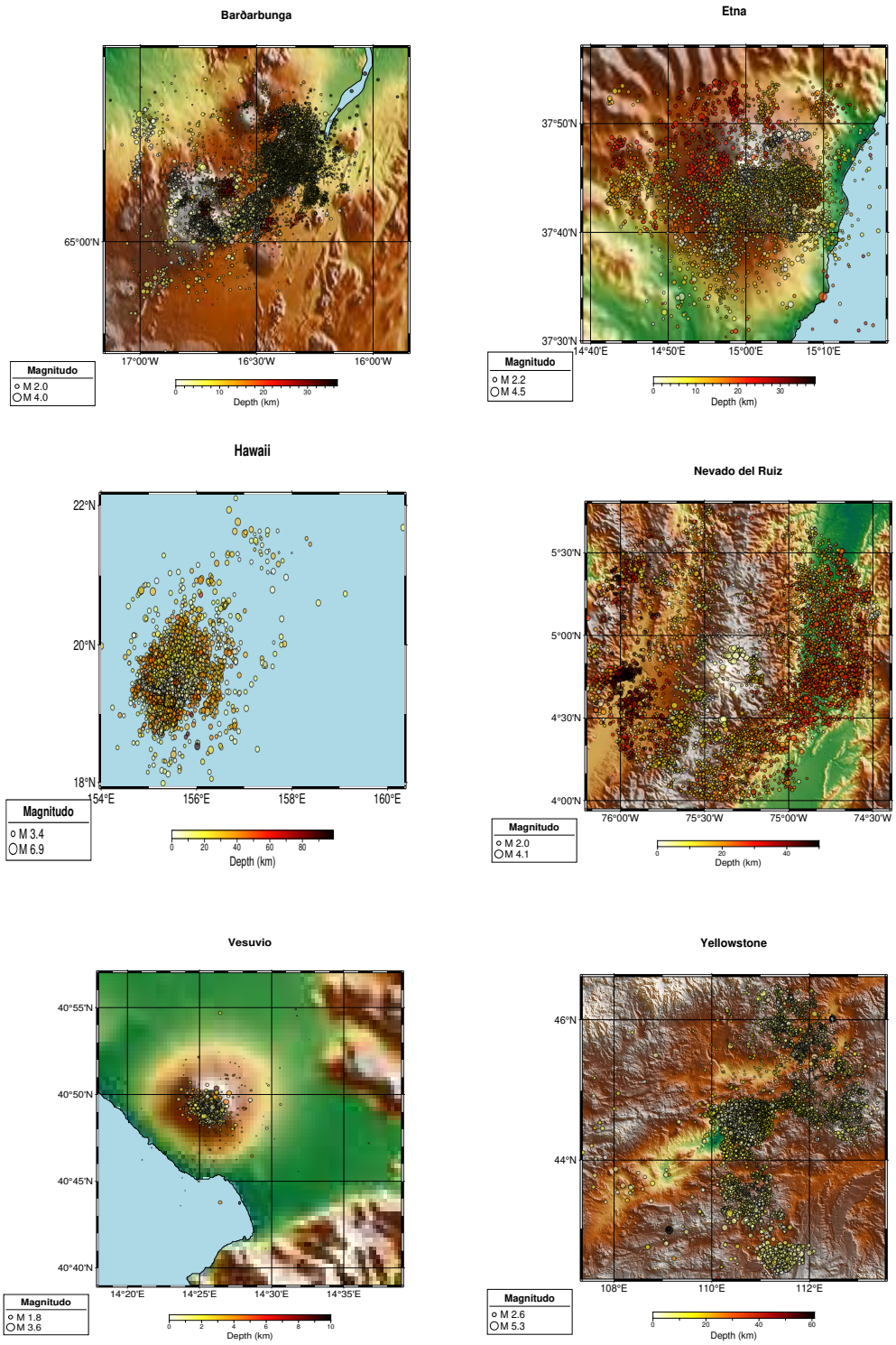


Fig. 2 Epicenters maps of the six volcanic systems: Bárðarbunga, Etna, Hawaii (Mauna Loa–Kīlauea), Nevado del Ruiz, Vesuvio, and Yellowstone. The circle size is proportional to the magnitude, whereas the color code represents the depth of the earthquake.

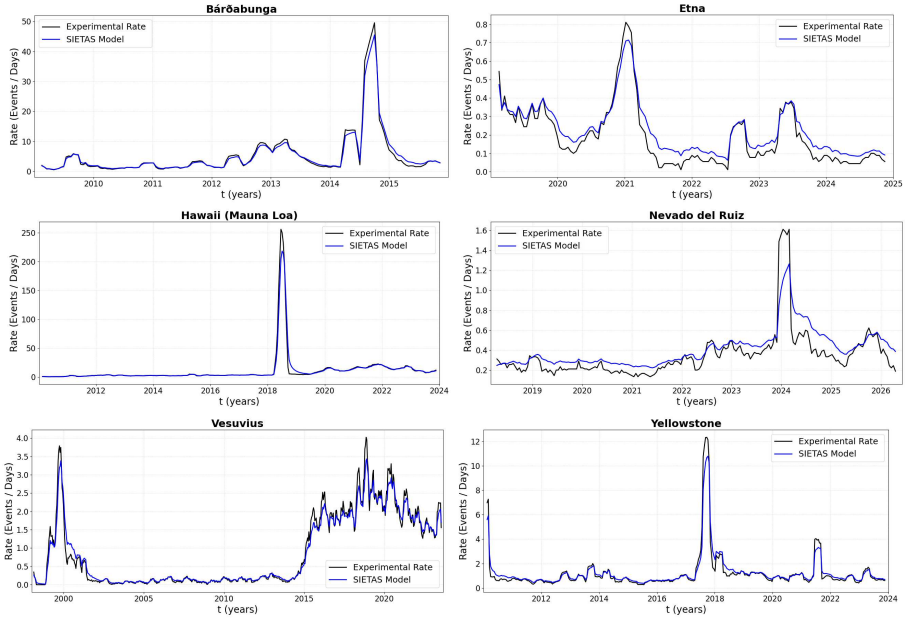


Fig. 3 Comparison between the experimental and theoretical earthquake occurrence rates for the six analyzed volcanic systems. The black solid line represents the experimental seismic rate calculated using a 90-day moving time window. The blue solid line indicates the theoretical rate predicted by the SIETAS model, using the estimated parameter values reported in the text. To ensure an objective and homogeneous comparison, the theoretical instantaneous intensity $\lambda(t)$ was integrated and smoothed over the identical 90-day window. Crimson vertical bars at the bottom indicate individual earthquake occurrences above the selected completeness magnitude (m_c). Note that despite the statistical AIC penalties currently affecting the Hawaii sequence due to local optimization limits, the graphical overlay shows an excellent first-order agreement with the historical seismicity across all catalogs.

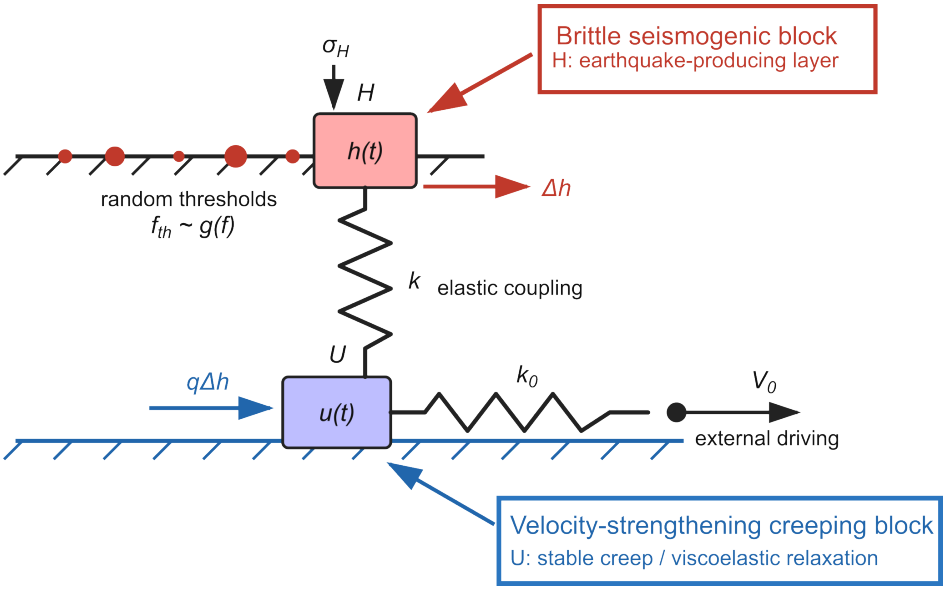


Fig. 4 Schematic representation of the two-block model used to motivate the temporal evolution of swarm triggering. The brittle seismogenic block H, located at $h(t)$, is elastically coupled through a spring of stiffness k to the stably creeping or viscoelastic block U, located at $u(t)$. The block U is driven by the external loading system $k_0 V_0$. The model provides a constitutive interpretation of the temporal kernel but does not imply a unique microscopic failure mechanism.